Nanoscale

Tethered Molecular Redox Capacitor for Nanoconfinement-Assisted Electrochemical Signal Amplification

Journal:	*Nanoscale*
Manuscript ID	NR-ART-09-2019-008136.R1
Article Type:	Paper
Date Submitted by the Author:	28-Oct-2019
Complete List of Authors:	Kang, Mijeong; Korea Institute of Materials Science, Mun, Chae-Won; Korea Institute of Materials Science, Jung, Ho Sang; Korea Institute of Materials Science, Ansah, Iris; Korea Institute of Materials Science Kim, Eunkyoung ; University of Maryland, IBBR Yang, Haesik; Pusan National University, Department of Chemistry Payne, Gregory; University of Maryland Biotechnology Institute, Center for Biosystems Research Kim, Dong-Ho; Korea Institute of Materials Science, Advanced Functional Thin Films Dep Park, Sung-Gyu; Korea Institute of Materials Science,

Tethered Molecular Redox Capacitor for Nanoconfinement-Assisted Electrochemical Signal Amplification

Mijeong Kang, ChaeWon Mun, Ho Sang Jung, Iris Baffour Ansah, Eunkyoung Kim, Haesik Yang, Gregory F. Payne, Dong-Ho Kim,* and Sung-Gyu Park**

Dr. M. Kang, C. Mun, Dr. H. S. Jung, I. B. Ansah, Dr. D.-H. Kim, Dr. S.-G. Park
Advanced Nano-Surface Department, Korea Institute of Materials Science (KIMS), Changwon, Gyeongnam 51508, South Korea
E-mail: mijeongkang@kims.re.kr, dhkim2@kims.re.kr, sgpark@kims.re.kr.

Dr. E. Kim, Prof. G. F. Payne
Institute for Bioscience and Biotechnology Research, University of Maryland, College Park, MD 20742, USA

Prof. H. Yang
Department of Chemistry, Pusan National University, Busan 46241, South Korea

Abstract

Nanostructured materials offer the potential to drive future developments and applications of electrochemical devices, but are underutilized because their nanoscale cavities can impose mass transfer limitations that constrain electrochemical signal-generation. Here, we report a new signal-generating mechanism that employs a molecular redox capacitor to enable nanostructured electrodes to amplify electrochemical signals even without enhanced reactant mass transfer. The surface-tethered molecular redox capacitor engages the diffusing reactants and products in redox-cycling reactions with the electrode. Such redox-cycling reactions are facilitated by the nanostructure that increases the probabilities of both reactant–electrode and product–redox-capacitor encounters (i.e., nanoconfinement effect), resulting in substantial signal amplification. Using redox-capacitor-tethered Au nanopillar electrodes, we demonstrate improved sensitivity for measuring pyocyanin (bacterial metabolite). This study paves a new way of using the nanostructured materials in electrochemical applications by engineering the reaction pathway within the nanoscale cavities of the materials.

1. Introduction

Nanostructured materials for electrochemical applications have led to new discoveries and advances in biological/chemical sensing,[1-3] energy generation/storage,[4-6] and information processing.[7] Many of the novel or improved performances of nanostructured electrodes are attributed to their structural features. Of particular interest is nanoconfinement in which a reactant enters a nanoscale cavity, resides in the cavity for a long time, and frequent collisions with the cavity surface enhances the probability of an electrochemical reaction.[8, 9] Nanoconfinement has driven the development of next-generation electrochemical devices like enzyme-free glucose sensors.[10]

Nanoconfinement, however, acts as a double-edged sword; while it provides high surface area for electrochemical reactions, it often imposes mass transfer limitations that impedes the reactant's entry into, and the product's escape from, the nanostructured cavity.[1, 11, 12] As schematically represented in **Figure 1a**, once the "nanoconfined" reactant reacts (i.e., exchanges electron) at the electrode, it cannot react again upon subsequent collisions with the electrode. This results in no further benefit of the nanoconfinement effect for the electrochemical signal.

Herein, we report the development of an additional signal-generating mechanism to enable the nanostructured electrodes to amplify electrochemical signals even without enhancing the efficiency of reactant transport into the nanostructured cavity of the electrode. We envision that, if the product's redox state can be cycled back to that of the reactant in the nanoscale cavity of the electrode, it can exchange electrons again with the electrode upon subsequent reactant–electrode collisions and generate an amplified signal. For this, we employ a "molecular redox capacitor"—a molecule that can accept, store, and donate electrons to provide an additional electron exchange mechanism. Specifically, the molecular redox capacitor engages a product in repetitive redox-cycling reactions with the electrode and generates an amplified electrochemical signal. As illustrated in **Figure 1b**, a catechol/*o*-quinone redox couple is employed as a molecular redox capacitor because of its reversible and rapid charging and discharging. We tethered this molecular redox capacitor to the electrode to localize its redox-cycling activity adjacent to the electrode region where the reactant is consumed and the product is formed; this minimizes the diffusional distance required for redox cycling. **Figure 1c** illustrates that such a redox-cycling reaction via the tethered redox capacitor is expected to occur more frequently within the nanostructured electrode because the probabilities of both the reactant–electrode encounter and the product–redox-capacitor encounter are likely increased by the nanoconfinement effect.[13] Thus, electrochemical signals should be

amplified by the synergistic actions of the molecular redox capacitor and the nanoconfinement effect.

We report that the molecular redox capacitor enables redox-cycling-based signal amplification for short and tall Au nanopillar electrodes and demonstrate these capabilities for the detection of pyocyanin (PYO, a redox-active biomarker of *Pseudomonas aeruginosa* infection). We show this amplification results from both the nanoconfinement and the capacitor's redox-cycling activities, and this signal enhancement is sensitive to nanoscale differences in the electrode structure.

2. Results and Discussion

2.1. Fabrication and Characterization of Nanopillar Electrodes. Au nanopillar electrodes were fabricated by Au deposition onto polymer (polyethylene terephthalate, PET) nanopillar substrates (see fabrication details in the Experimental Section and Figure S1 in Supporting Information).[14-18] As a control, a flat Au/PET electrode was fabricated by depositing Au onto the as-received PET substrate. **Figure 2** shows the scanning electron microscopy images of the Au-deposited short and tall PET nanopillar substrates. The short Au/PET nanopillars (henceforth referred as short nanopillars) are 306 ± 28 nm in height and are separated by 105 ± 75 nm at an areal density of 41 ± 4 μm^{-2}. The tall Au/PET nanopillars (tall nanopillars) are 441 ± 36 nm high (i.e., 1.4 times higher than the short nanopillars) and are separated by 119 ± 92 nm at an areal density of 43 ± 3 μm^{-2}. The electrochemically active surface areas (EASAs) of the nanopillar electrodes, as well as that of the flat electrode, were evaluated with a standard electrochemical procedure (Figure S2 in Supporting Information).[19] The EASAs of the short and tall nanopillar electrodes are 6.6 ± 1.0 and 8.6 ± 1.1 times larger than that of the flat electrode, respectively. For the nanopillar electrodes, the EASA ratio (short:tall = 1:1.3) is comparable to the ratio of the nanopillar heights (short:tall = 1:1.4).

2.2. Construction of the Molecular Redox Capacitor System. To demonstrate our approach to signal amplification in nanostructured electrodes using a molecular redox capacitor which is catechol/*o*-quinone (Cat^{RED}/Cat^{OX}, shortened to Cat), we employed two diffusible reactants, pyocyanin (PYO) and ferrocene (Fc) (**Figure 3a**).[20] PYO is a redox-active bacterial metabolite with a standard redox potential ($E°$) of −0.25 V (vs. Ag/AgCl).[21] Fc is a well-characterized and well-behaved redox probe with $E° \approx +0.25$ V. Cat^{RED}/Cat^{OX} has $E° \approx +0.2$ V,[22] which is intermediate between those of PYO and Fc, thereby thermodynamically enabling the redox reaction with each redox reactant (see below).

As suggested in the thermodynamic plots in **Figure 3b**, Cat regenerates the oxidized state of PYO when it is discharged while it regenerates the reduced state of Fc when it is charged; redox-cycling system is formed of electrode–PYO–Cat^{OX} and electrode–Fc–Cat^{RED}. When the electrode is polarized at a potential more negative than −0.25 V, PYO (initially in the oxidized state, PYO^{OX}) is reduced (i.e., PYO^{RED}) at the electrode. This PYO^{RED} charges the electron-deficient Cat^{OX} and turns back into PYO^{OX}, which is reduced again at the electrode. A PYO molecule is thereby repeatedly reduced (by an electrode) and oxidized (by Cat^{OX}) and the PYO reduction current is thus amplified. The redox-cycling system involving PYO only charges Cat, whose capacity to accept electrons from PYO^{RED} consequently decreases, limiting the repeated use of Cat. Such a limitation is overcome by the counteraction of Fc on the redox state of Cat. When a potential more positive than +0.25 V is applied to the electrode, Fc (initially in the reduced state, Fc^{RED}) is oxidized (i.e., Fc^{OX}) at the electrode, discharges the electron-rich Cat^{RED} and returns to Fc^{RED}, which is re-oxidized at the electrode, amplifying the Fc oxidation current. In the redox-cycling system involving Fc, Cat restores its discharged state. Therefore, the repetitive and reproducible use of Cat is enabled by such a full redox-cycling system involving both PYO and Fc.

To ensure that the molecular redox capacitor immediately react with the product that diffuses from the electrode, we tethered the molecular redox capacitor closely to the electrode surface via an electrically inert molecular tether rather than dissolving it in a solution. As illustrated in **Figure 3c**, we first formed a hydroxy-terminated self-assembled monolayer (SAM) using 6-mercapto-1-hexanol (MCH). Catechol was electrochemically oxidized at this MCH/Au electrode to generate *o*-quinone, which is highly reactive,[23] enabling its conjugation to the hydroxyl terminal[24] of MCH or its polymerization (polycatechol has E° of ~0 V,[25] which enables redox reactions with both PYO and Fc) and adsorption onto the MCH layer (see Figure S3 Supporting Information for details). This surface-tethered Cat (or polycatechol) can be directly charged and discharged by the underlying electrode rather than redox-cycling with PYO and Fc; however, the direct Cat reduction and oxidation are insignificantly observed and the amplification of the PYO and Fc signals after the Cat graft indicates that the Cat participates in the redox reactions with PYO and Fc (see below).

2.3. Electrochemical Signature of Tethered Molecular Redox Capacitor and Redox-Cycling Reaction. The formation of redox-cycling system based on a molecular redox capacitor was electrochemically verified, as demonstrated in **Figure 4**. Electrochemical signals of PYO and Fc were measured at the MCH/Au tall nanopillar electrode before and after the Cat graft. First, **Figure 4a** shows the original (upper) and background-subtracted (lower) cyclic voltammogram of a buffered solution

containing PYO, as recorded before the Cat graft. The PYO signal is observed around −0.25 V. When Fc was added to the PYO solution (**Figure 4b**, red), an additional signal appeared at +0.25 V. The addition of Fc did not induce a substantial change in the PYO signal, indicating negligible interaction between PYO and Fc. After the Cat graft, in a PYO-only solution (**Figure 4c**, blue), the PYO reduction peak current was amplified by a factor of 1.7 whereas the PYO oxidation peak current was similar, compared with the PYO signal in Figure 4a. This asymmetric signal amplification evinces the redox reaction between PYO^{RED} and Cat^{OX}. In the cathodic potential scan (from 0 to −0.45 V), the initial PYO^{OX} is reduced to PYO^{RED} at the electrode, oxidized back to PYO^{OX} by Cat^{OX} and then re-reduced at the electrode, through which only the reduction current is amplified. Because PYO^{RED} is oxidized by Cat^{OX} in the cathodic scan before being oxidized at the electrode in the following anodic scan (from −0.45 to 0 V), no substantial changes in the apparent PYO oxidation current were observed. When Fc was added to this PYO solution (**Figure 4d**, green), asymmetric amplification of the Fc signal was observed, indicating that the redox reaction occurred between Fc^{OX} and Cat^{RED}; Fc^{RED} was oxidized at the electrode, reduced back by Cat^{RED} and re-oxidized at the electrode, amplifying only the Fc oxidation peak current by a factor of ~2.9 (vs. the Fc signal in Figure 4b). Notably, the PYO reduction peak current was further amplified by a factor of 2.1 in this solution (i.e., 3.9 times greater than the PYO signal in Figure 4a). This amplification was due to the transformation of Cat^{RED} to Cat^{OX} during the Fc-involving redox-cycling reaction, which increased the amount of Cat^{OX} participating in the PYO-involving redox-cycling reaction.

To quantitatively characterize the asymmetric signal amplification by the Cat-based redox-cycling reactions, we define the amplification ratio (AR) and rectification ratio (RR) (**Figure 4e**) by slightly modifying the previously reported metrics.[26] These two metrics were used as measures of the redox cycle efficiency of flat, short nanopillar, and tall nanopillar electrodes, as discussed below.

2.4. Effect of Nanostructures on Redox-Cycling Reaction. To observe how the electrode nanostructure affects the efficiency of the redox-cycling reaction based on a molecular redox capacitor, we compared the PYO and Fc signals measured at the Cat-grafted flat, short nanopillar, and tall nanopillar electrodes. As illustrated in **Figure 5a**, we first ensured that the electrode surface was fully functionalized with Cat by repeating the Cat graft reactions until the PYO and Fc signals were saturated. **Figure 5b** shows the background-subtracted cyclic voltammograms of PYO and Fc recorded after each Cat graft to the flat, short nanopillar, and tall nanopillar electrodes (see Figure S4 in Supporting Information for the original cyclic voltammograms). The PYO and Fc signals were saturated after the second, third, and sixth Cat graft reaction for the flat, short nanopillar, and tall nanopillar electrodes, respectively. The final PYO

reduction peak currents are 1.2 and 3.9 μA at the short and tall nanopillar electrodes, which are 6 and 19.5 times greater than that measured at the flat electrode (0.2 μA), respectively. **Figure 5c** shows that the AR and RR for the PYO signals are enhanced by the nanopillar electrodes and that greater ratios are achieved by the tall nanopillar electrode, implying greater efficiency of the redox-cycling reaction. [Note: similar variations in the AR and RR for the Fc signals are shown in Figure S5 in Supporting Information.] In the case of the flat electrode, the AR and RR approached unity, indicating an insignificant redox-cycling reaction. We speculate that PYO, after being reduced at the flat electrode, readily diffuses away from the electrode surface and rarely encounters Cat.

The aforementioned difference in the redox reactant signals appears to be attributable to the difference in electrode surface areas. As shown in **Figure 5d**, the PYO reduction peak current increases with increasing the electrode surface area both before and after Cat graft; however, it is not linearly proportional to the electrode surface area. In **Figure 5e**, to clearly show that the nanoconfinement effect in the nanopillar electrodes indeed plays a critical role in the signal amplification, the PYO reduction peak current is normalized by the electrode surface area. Before the Cat graft, the current density of the PYO reduction peak was higher at the flat electrode (0.8 $\mu A/cm^2$) than at the nanopillar electrodes (0.3 and 0.7 $\mu A/cm^2$ for the short and tall nanopillar electrodes, respectively). Such a decrease in the current density for the diffusion-controlled reaction by nanopillar electrodes is generally observed for nanostructured electrodes.[27, 28] After the final Cat graft, the current density obtained from the short nanopillar electrode increased to 0.9 $\mu A/cm^2$, which is comparable to that obtained from the flat electrode (1.0 $\mu A/cm^2$). Surprisingly, the tall nanopillar electrode provided the highest current density (2.5 $\mu A/cm^2$), implying that the redox-cycle-assisted signal amplification occurred most efficiently at the tall nanopillar electrode. PYO is less likely to escape from the cavity in the tall nanopillar electrode than from that in the short nanopillar electrode. Thus, PYO collides with Cat and with the electrode more frequently in the tall nanopillar electrode and, as a result, the PYO signal amplification is further improved. [Note: similar variations in the current and current density of Fc oxidation peaks are shown in Figure S5.]

Figure 5 conveys two conclusions. From a methods standpoint, the molecular redox capacitor offers a new approach to characterizing and exploiting the structural features of nanostructured electrodes, especially their nanoconfinement effects on electrochemical signals. It has been considered that the signal amplification based on the nanoconfinement effect is only available for the electrochemical reactions of

moderately slow electron-transfer kinetics. But, our method shows that the electrochemical reactions of Fc and PYO having fast electron-transfer kinetics (Figure S6 in the Supporting Information) can be amplified by the nanostructured electrodes, which we believe opens a new way of applying the nanostructured electrodes. From a materials standpoint, the efficiency of the redox-cycling reaction can be improved by tailoring the electrode structure at the nanoscale.

2.5. Applications. As a model application, we measured the concentration of PYO in buffered and diluted serum (as a model body fluid) solutions. PYO is a metabolite solely produced and secreted by a ubiquitous bacterium, *Pseudomonas aeruginosa* (*P. aeruginosa*), one of the major pathogens associated with sepsis and clinical airway diseases (e.g., acute pneumonia, chronic lung infections) in cystic fibrosis patients.[29-31] This pathogen is fatal especially to immunocompromised individuals and has developed resistance to multiple antibiotics; therefore, the early detection of a *P. aeruginosa* infection is critical to avoid a serious condition that leads to therapeutic challenges.[32] PYO has recently emerged as a promising biomarker in the electrochemical diagnostic of *P. aeruginosa* infection.[33-40] In particular, the PYO signal lies outside the potential window of common redox-active interferants (e.g., ascorbate, uric acid), which enables direct electrochemical detection of PYO with appropriate selectivity.[39, 41]

To further improve the PYO signal amplification, we employed linear sweep voltammetry (LSV) followed by the catechol discharging process. **Figure 6** shows the PYO signals measured in the presence of Fc at the Cat-grafted tall nanopillar electrode using cyclic voltammetry (CV) and the LSV without and with the Cat pre-discharging process (i.e., the application of +0.4 V before running LSV). [Note: LSV plots are presented after background-subtraction as shown in Figure S7 in Supporting Information.] Similar PYO reduction peak currents were measured by CV (3.9 μA) and the LSV without Cat pre-discharging (3.8 μA). After 30 s of the Cat pre-discharging process, the PYO reduction peak current increased to 5.5 μA; the magnitude of this increment was dependent on the pre-discharging time (Figure S7). During the Cat pre-discharging process, Fc is oxidized at the electrode and then discharges Cat, increasing the electron-accepting capacity of Cat for the PYO-involving redox-cycling reaction. This approach provides a convenient way of controlling and enhancing the extent of Cat discharging (i.e., by varying the discharging time) and was thus used in subsequent PYO measurements.

We evaluated the sensitivities of PYO measurements conducted with the Cat-grafted flat, short nanopillar, and tall nanopillar electrodes. **Figure 7a** shows the background-subtracted linear sweep voltammograms recorded with the electrodes in buffered solutions in which the concentrations of both PYO and Fc were

varied from 50 nM to 1 μM (see Figure S8 in Supporting Information for the original linear sweep voltammograms). [Note: the concentration range was determined by considering the previously reported PYO concentrations in clinical samples (i.e., from a few tens to 130 μM)[42] and the serum dilution in our study (i.e., 100-times dilution).] **Figure 7b** shows the PYO reduction peak currents plotted as a function of the PYO concentration, along with the linear fitting results for the low-concentration regions. The nanopillar electrodes amplify the PYO signals and ultimately improve the measurement sensitivity by decreasing the limit of detection (LOD) from 250.8 nM (by flat electrodes) to 61.0 nM (by short nanopillar electrodes, a 3.7-fold decrease) and 16.3 nM (by tall nanopillar electrodes, a 15.4-fold decrease), as shown in **Figure 7c**. When the same concentrations of PYO and Fc were spiked into the 100-times-diluted serum solutions, weaker PYO signals were recorded (**Figure 7d,e**) compared with those recorded in the buffered solutions, likely because the complex serum components partially blocked the electrode surface. More importantly, the LSV from serum solution showed no apparent interfering signal in the potential range of the PYO signal (Figure S8 in Supporting Information). In the serum samples, nanopillar electrodes amplify the PYO peak current and lower the LOD from 398.1 nM (by flat electrodes) to 206.3 nM (by short nanopillar electrodes, a 1.9-fold decrease) and 31.9 nM (by tall nanopillar electrodes, a 12.4-fold decrease) (**Figure 7f**), which correspond to 39.8, 20.6, and 3.2 μM in undiluted serum, respectively (see Table S1 for comparison with the LODs obtained from other electrochemical detection methods). Figure 7 clearly demonstrates that the nanopillar electrodes, functionalized with a molecular redox capacitor, provides practical benefits in the electrochemical sensing.

3. Conclusions

In summary, we developed a redox-capacitor-based electrochemical system to utilize the nanoconfinement effect for amplifying electrochemical signals with nanostructured electrodes. We chemically tethered the catechol-based molecular redox capacitor to Au nanopillar electrodes and flat electrodes. The tethered capacitor redox-cycles with the reactants, pyocyanin and ferrocene, resulting in their signal amplification and this signal amplification was especially important for the nanopillar electrodes (vs. flat electrodes) due to the nanoconfinement effect. In particular, tethering the molecular redox capacitor to the nanopillar electrodes provided improved sensitivity (i.e., lower LOD) for measuring pyocyanin. We believe this work demonstrates the potential of nanostructured electrodes to

provide improved electrochemical performances by designing the electron exchange reaction pathway within the nanoscale cavity in the nanostructured electrodes.

4. Experimental Section

Materials. Catechol, 1-hexanethiol, 6-mercapto-1-hexanol, and pyocyanin were purchased from Sigma-Aldrich. 1,1′-Ferrocenedimethanol and fetal bovine serum were acquired from Acros and from Millipore, respectively. The polyethylene terephthalate (PET) substrate was obtained from Toray. Deionized water (DIW, >18 MΩ·cm) was prepared with a Human UP (Human Corp.). All solutions were prepared in a phosphate buffer solution (0.1 M, pH ~7.2) except for the pyocyanin stock solution (10 mM), which was prepared in ethanol.

Fabrication and Characterization of Nanopillar Electrodes. PET substrates were treated with plasma using a home-built 13.56 MHz radio-frequency ion etching instrument. To produce short PET nanopillars, PET substrates were treated with CF_4 plasma (plasma power: 100 W) generated from a CF_4 gas flowing at 3 standard cubic centimeters per minute (sccm) under a chamber pressure of 56 mTorr for 2 min. For tall nanopillar PET substrates, an additional Ar plasma treatment (plasma power: 100 W, Ar flow rate: 3 sccm, chamber pressure: 32 mTorr, duration: 1 min) was followed by the same CF_4 plasma treatment. Subsequently, Au was deposited to a thickness of 150 nm onto PET nanopillar substrates by a sputtering system at a deposition rate of 2.0 Å/s under a working pressure of 7 mTorr. Flat Au electrodes were fabricated by directly depositing Au onto an as-received PET substrate (i.e., without plasma treatment) using the same sputtering method. The surface morphologies of the nanopillar substrates were characterized by field-emission scanning electron microscopy (JSM-6700F, JEOL). The cross-section of the nanopillar electrode was prepared and observed (tilted by 52°) with an ultra-high-resolution focused ion beam (Helios G4, FEI).

Surface Modification of Au Electrodes. Prior to Au surface modifications, all of the Au/PET electrodes were assembled into electrochemical cells and cleaned using a standard electrochemical process (see details in the following subsection). Next, the Au surface was exposed to a 2 mM mercaptohexanol (MCH) solution (freshly prepared in buffer) for 2 h at room temperature and then thoroughly rinsed with DIW. At the MCH/Au electrodes, catechol (2 mM, freshly prepared in deaerated buffer) was electrochemically oxidized at a constant potential of +0.3 V for 1 min while N_2 gas passed through the solution. The

catechol-grafted electrodes were thoroughly rinsed with 50% ethanol to remove the physisorbed catechol and *o*-quinone.

Electrochemical Measurements. All electrochemical measurements were carried out using a potentiostat (ZIVE SP2, Wonatech) equipped with a homemade electrochemical cell that held the Au/PET electrodes, Ag/AgCl (in 3 M NaCl) as a reference electrode, and Pt wire as a counter electrode. In the cell, the Au surface with a geometric area of 0.13 cm^2 was exposed to the solution. The electrode potential is reported vs. Ag/AgCl. To clean the Au electrode surface, we conducted cyclic voltammetry (CV) by scanning the potential between 0 and +1.1 V at a scan rate of 0.05 V/s with the electrodes in buffer solution until a reproducible cyclic voltammogram was obtained. For measuring the pyocyanin and ferrocene signals, CV was performed by scanning the potential between +0.45 and −0.45 V at 0.2 V/s in three cycles; the cyclic voltammograms at the second cycle are presented. Linear sweep voltammetry (LSV) was performed from 0 to −0.45 V at 0.2 V/s with or without the catechol pre-discharging step (imposing +0.4 V for 10, 20, or 30 s). The electrode functionalized with the molecular redox capacitor were re-used for a series of measurement with an electrode washing in 50% ethanol between each measurement. Clean electrode surface was verified by the featureless background signal measured after electrode washing and the reproducibility of the electrodes was verified by the consistent measurement of pyocyanin and ferrocene signals. For estimating the limit of detection (LOD), measurements were conducted in triplicate using three individual Au/PET electrodes for each substrate (flat, short nanopillar and tall nanopillar). The LOD was calculated as 3σ/sensitivity, where σ is the standard deviation of the current of a blank buffer solution and the sensitivity is the slope of the linear fit.

Acknowledgements

This work was supported by Fundamental Research Program (PNK 6070) of the Korean Institute of Materials Science (KIMS). This work was also supported by the "Ministry of Trade, Industry and Energy (Grant N0002310)" and the United States National Science Foundation (ECCS-1807604). M. Kang thanks Dr. Seunghun Lee for valuable discussion and manuscript preparation.

References

1. N. Wongkaew, M. Simsek, C. Griesche and A. J. Baeumner, *Chem Rev*, 2019, **119**, 120-194.
2. A. Chen and S. Chatterjee, *Chem. Soc. Rev.*, 2013, **42**, 5425-5438.
3. C. Z. Zhu, G. H. Yang, H. Li, D. Du and Y. H. Lin, *Anal. Chem.*, 2015, **87**, 230-249.
4. M. Zhou, Y. Xu and Y. Lei, *Nano Today*, 2018, **20**, 33-57.
5. P. Trogadas, V. Ramani, P. Strasser, T. F. Fuller and M. O. Coppens, *Angew. Chem. Int. Ed.*, 2016, **55**, 122-148.
6. L. Yu, H. Hu, H. B. Wu and X. W. Lou, *Adv. Mater.*, 2017, **29**, 1604563.
7. R. Waser, R. Dittmann, G. Staikov and K. Szot, *Adv. Mater.*, 2009, **21**, 2632-2663.
8. S. Park, H. C. Kim and T. D. Chung, *Analyst*, 2012, **137**, 3891-3903.
9. M. Seo and T. D. Chung, *Curr. Opin. Electrochem.*, 2019, **13**, 47-54.
10. F. Xiao, L. Wang and H. W. Duan, *Biotechnol. Adv.*, 2016, **34**, 234-249.
11. J. Snyder, I. McCue, K. Livi and J. Erlebacher, *J. Am. Chem. Soc.*, 2012, **134**, 8633-8645.
12. D. B. Luo, L. Z. Wu and J. F. Zhi, *Acs Nano*, 2009, **3**, 2121-2128.
13. R. J. White and H. S. White, *Anal. Chem.*, 2005, **77**, 214 A-220 A.
14. R. Di Mundo, M. Troia, F. Palumbo, M. Trotta and R. d'Agostino, *Plasma Process. Polym.*, 2012, **9**, 947-954.
15. S. Lee, E. Byeon, S. Jung and D. G. Kim, *Sci. Rep.*, 2018, **8**, 14063.
16. J. Yun, W. Wang, S. M. Kim, T.-S. Bae, S. Lee, D. Kim, G.-H. Lee, H.-S. Lee and M. Song, *Energ Environ. Sci.*, 2015, **8**, 932-940.
17. S.-G. Park, C. Mun, X. Xiao, A. Braun, S. Kim, V. Giannini, S. A. Maier and D.-H. Kim, *Adv. Funct. Mater.*, 2017, **27**, 1703376.
18. X. Wang, S. G. Park, J. Ko, X. Xiao, V. Giannini, S. A. Maier, D. H. Kim and J. Choo, *Small*, 2018, **14**, 1801623.
19. J. C. Hoogvliet, M. Dijksma, B. Kamp and W. P. van Bennekom, *Anal. Chem.*, 2000, **72**, 2016-2021.
20. E. Kim, T. Gordonov, W. E. Bentley and G. F. Payne, *Anal. Chem.*, 2013, **85**, 2102-2108.
21. D. L. Bellin, H. Sakhtah, J. K. Rosenstein, P. M. Levine, J. Thimot, K. Emmett, L. E. Dietrich and K. L. Shepard, *Nat. Commun.*, 2014, **5**, 3256.
22. E. Kim, W. T. Leverage, Y. Liu, I. M. White, W. E. Bentley and G. F. Payne, *Analyst*, 2014, **139**, 32-43.

23. T. Kashiwagi, F. Amemiya, T. Fuchigami and M. Atobe, *J. Flow Chem.*, 2012, **3**, 17-22.
24. M. Sugumaran, *Int. J. Mol. Sci.*, 2016, **17**, 1576.
25. J. Bai, X. Bo, B. Qi and L. Guo, *Electroanal.*, 2010, **22**, 1750-1756.
26. Y. Liu, E. Kim, I. M. White, W. E. Bentley and G. F. Payne, *Bioelectrochemistry*, 2014, **98**, 94-102.
27. K. Sanger, O. Durucan, K. Wu, A. H. Thilsted, A. Heiskanen, T. Rindzevicius, M. S. Schmidt, K. Zor and A. Boisen, *ACS Sens.*, 2017, **2**, 1869-1875.
28. R. Szamocki, S. Reculusa, S. Ravaine, P. N. Bartlett, A. Kuhn and R. Hempelmann, *Angew. Chem. Int. Ed.*, 2006, **45**, 1317-1321.
29. G. W. Lau, D. J. Hassett, H. Ran and F. Kong, *Trends Mol. Med.*, 2004, **10**, 599-606.
30. J. L. Vincent, J. Rello, J. Marshall, E. Silva, A. Anzueto, C. D. Martin, R. Moreno, J. Lipman, C. Gomersall, Y. Sakr, K. Reinhart and E. I. G. o. Investigators, *JAMA-J. Am. Med. Assoc.*, 2009, **302**, 2323-2329.
31. R. B. Fick, Jr., *Chest*, 1989, **96**, 158-164.
32. P. D. Lister, D. J. Wolter and N. D. Hanson, *Clin. Microbiol. Rev.*, 2009, **22**, 582-610.
33. A. Buzid, F. Shang, F. J. Reen, E. O. Muimhneachain, S. L. Clarke, L. Zhou, J. H. Luong, F. O'Gara, G. P. McGlacken and J. D. Glennon, *Sci. Rep.*, 2016, **6**, 30001.
34. J. Elliott, O. Simoska, S. Karasik, J. B. Shear and K. J. Stevenson, *Anal. Chem.*, 2017, **89**, 6285-6289.
35. B. Ciui, M. Tertis, A. Cernat, R. Sandulescu, J. Wang and C. Cristea, *Anal. Chem.*, 2018, **90**, 7761-7768.
36. H. J. Sismaet, T. A. Webster and E. D. Goluch, *Analyst*, 2014, **139**, 4241-4246.
37. H. J. Sismaet, A. J. Pinto and E. D. Goluch, *Biosens. Bioelectron.*, 2017, **97**, 65-69.
38. R. Burkitt and D. Sharp, *Electrochem. Commun.*, 2017, **78**, 43-46.
39. F. A. Alatraktchi, J. S. Noori, G. P. Tanev, J. Mortensen, M. Dimaki, H. K. Johansen, J. Madsen, S. Molin and W. E. Svendsen, *Plos One*, 2018, **13**, e0194157.
40. T. Seviour, L. E. Doyle, S. J. Lauw, J. Hinks, S. A. Rice, V. J. Nesatyy, R. D. Webster, S. Kjelleberg and E. Marsili, *Chem. Commun.*, 2015, **51**, 3789-3792.
41. F. A. Alatraktchi, H. K. Johansen, S. Molin and W. E. Svendsen, *Nanomedicine-Uk*, 2016, **11**, 2185-2195.
42. S. Hall, C. McDermott, S. Anoopkumar-Dukie, A. J. McFarland, A. Forbes, A. V. Perkins, A. K. Davey, R. Chess-Williams, M. J. Kiefel, D. Arora and G. D. Grant, *Toxins*, 2016, **8**, 236.

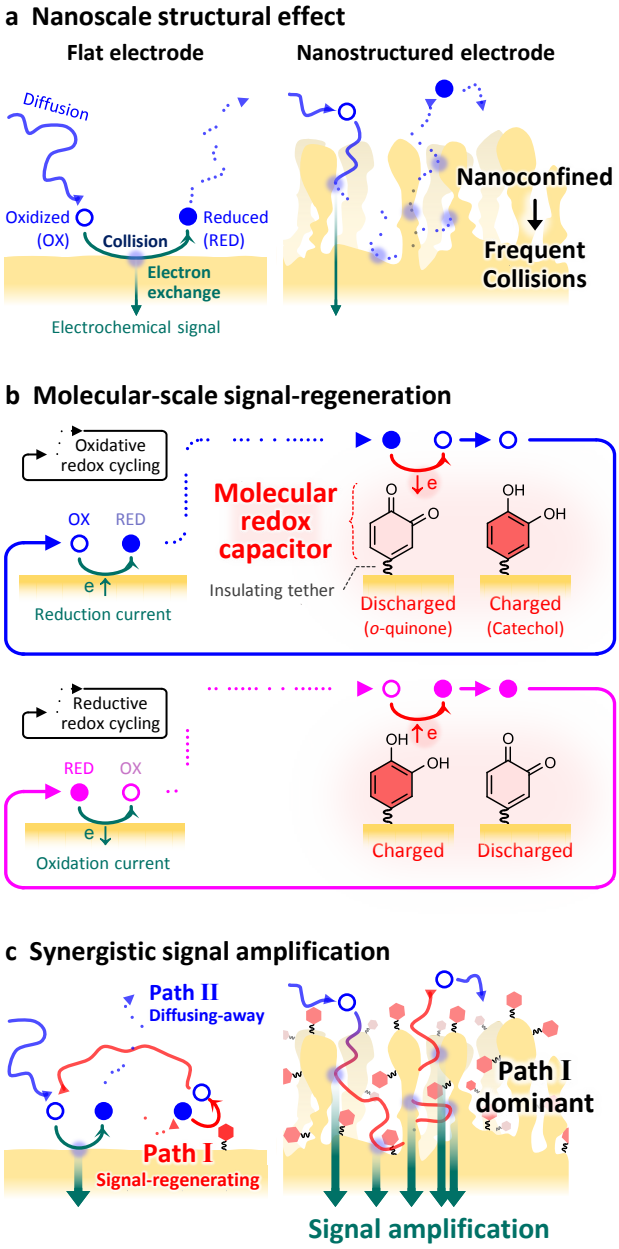

Figure 1. Tethered molecular redox capacitor for electrochemical signal amplification in a nanostructured electrode. (a) Once a molecular reactant enters the nanoscale cavity of a nanostructured electrode, it is easily confined and frequently collides with the electrode surface (the "nanoconfinement effect"). The reactant collision with a polarized electrode results in electron exchange. Frequent collisions in a nanostructured electrode do not result in multiple electron exchanges. **(b)** After the reactant is reduced (upper) or oxidized (lower) at the electrode, the product diffuses and encounters a molecular redox capacitor, a catechol/*o*-quinone redox couple, tethered to the electrode surface. The catechol/*o*-

quinone couple exchanges electrons with the product, cycling-back the redox state of the product to its initial state and thus enabling further electrochemical reaction upon subsequent collisions with the electrode (redox-cycling reaction). **(c)** Redox-cycling reaction can be facilitated by the nanoconfinement effect that can increase the frequencies of reactant–electrode and product–redox-capacitor collisions.

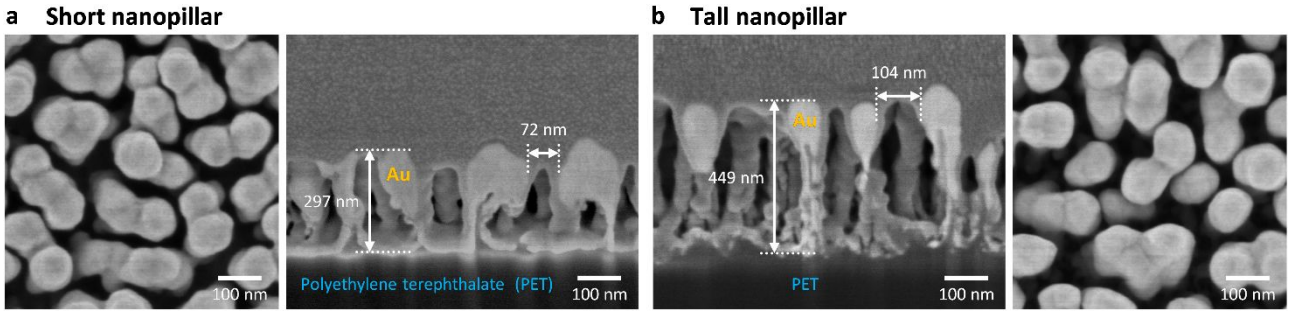

Figure 2. Structures of Au nanopillar electrodes. (a) Top (left) and cross-sectional (right) scanning electron microscopy images of a short nanopillar electrode. **(b)** Cross-sectional (left) and top (right) images of a tall nanopillar electrode. In the cross-sectional images, the heights and the interpillar distances of Au nanopillars are indicated.

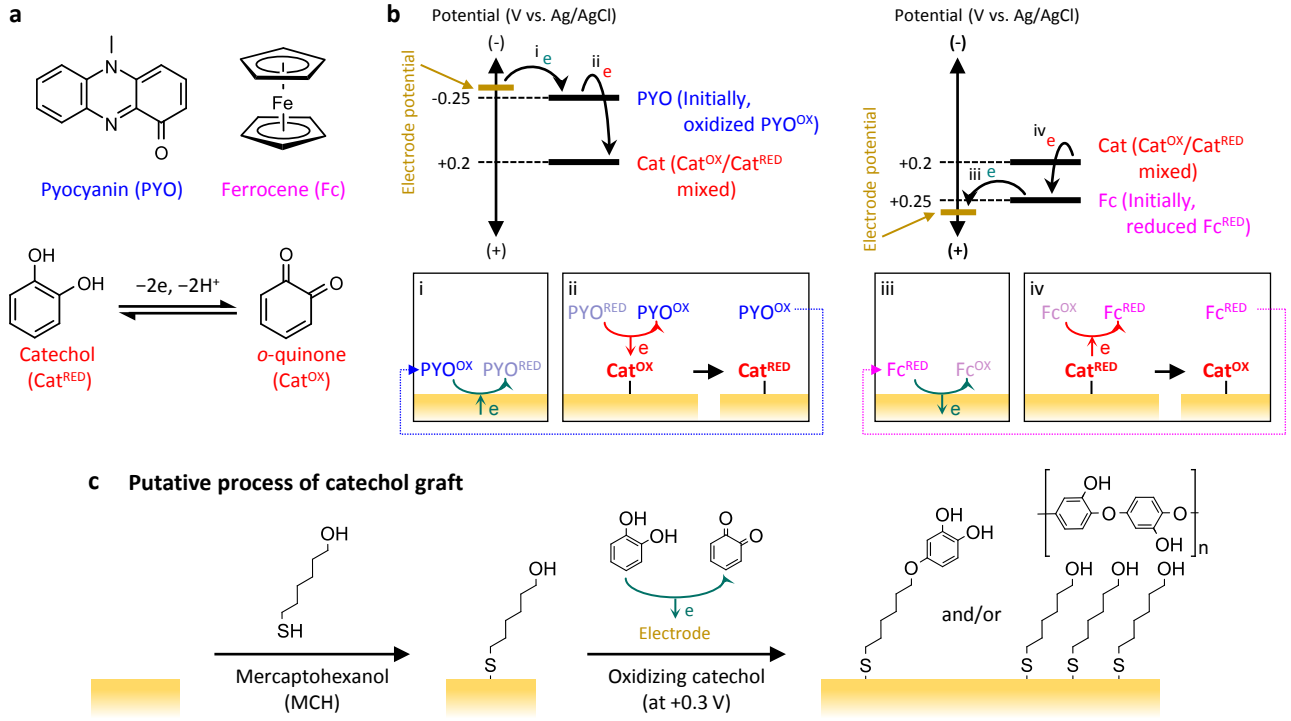

Figure 3. Construction of the molecular redox capacitor system. (**a**) As diffusible reactants, pyocyanin (PYO) and ferrocene (Fc) are used; as a molecular redox capacitor, catechol/*o*-quinone (Cat^{RED}/Cat^{OX}, Cat) is used. **(b)** At an electrode potential more negative than −0.25 V, PYO (initially in the oxidized state, PYO^{OX}) is reduced by the electrode to become PYO^{RED} (i). When encountering the electron-deficient Cat^{OX}, PYO^{RED} transfers its electrons to Cat^{OX}, thereby returning to PYO^{OX} (ii). This PYO^{OX} can again be reduced at the electrode. At an electrode potential more positive than +0.25 V, Fc (initially in the reduced state, Fc^{RED}) is oxidized (Fc^{OX}) at the electrode (iii) and gains an electron from the electron-rich Cat^{RED} to turn back into Fc^{RED} (iv), which can be reoxidized at the electrode. **(c)** To graft Cat onto the electrode surface, a self-assembled monolayer of mercaptohexanol (MCH) is formed on the electrode. At this electrode, catechol is oxidized to become highly unstable *o*-quinone. The putative chemical structures of the grafted Cat are shown.

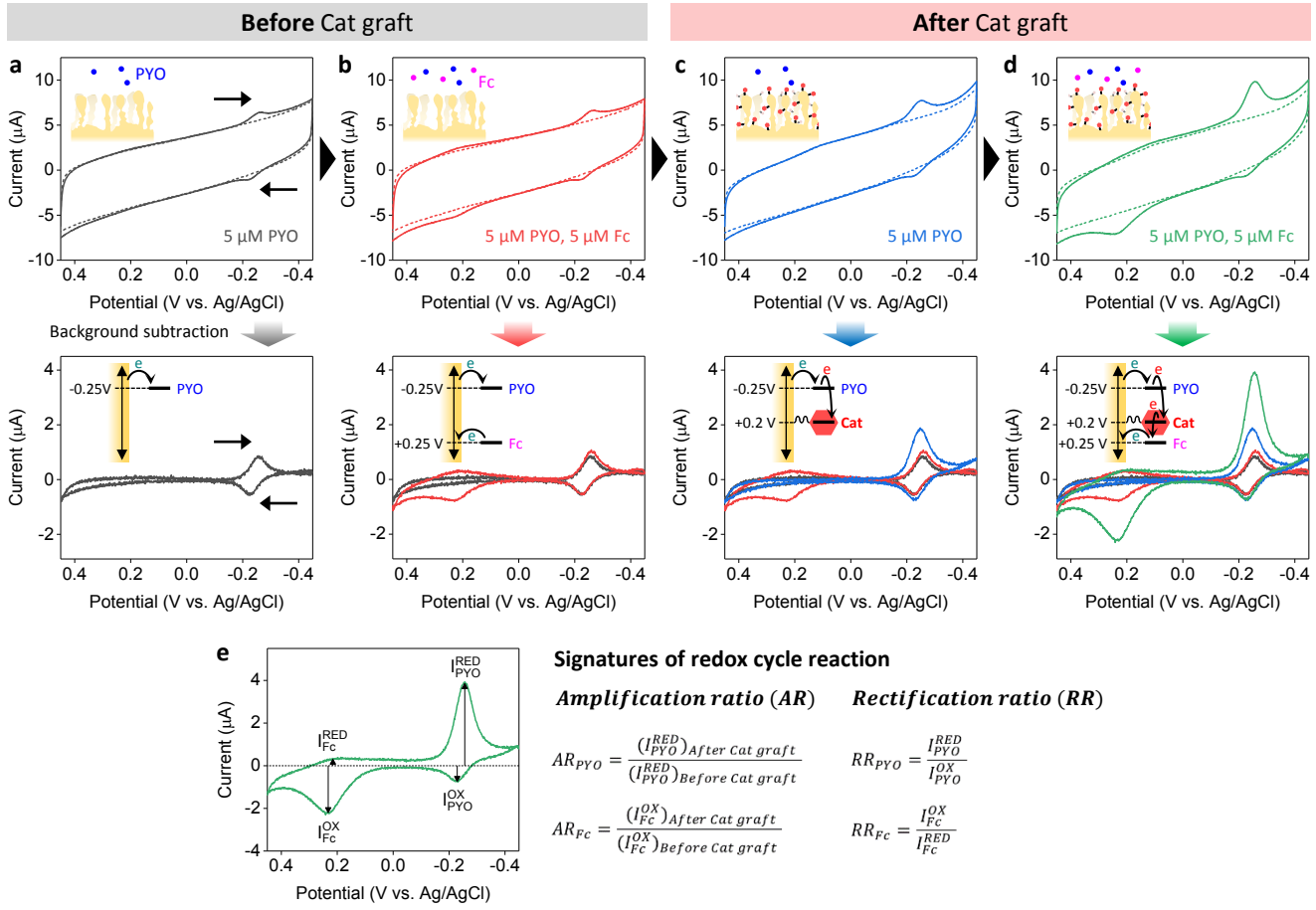

Figure 4. Electrochemical signatures of the redox-cycling system based on a tethered molecular redox capacitor. (a-d) Original cyclic voltammograms (upper) and the corresponding background-subtracted cyclic voltammograms (lower) recorded with the MCH/Au tall nanopillar electrode in solutions containing PYO only (a,c) and PYO and Fc (b,d) before (a,b) and after (c,d) the Cat graft. Dashed lines in the upper plots were measured in a blank buffer solution. **(e)** Definition of the amplification ratio (AR) and the rectification ratio (RR) for the PYO and Fc signals.

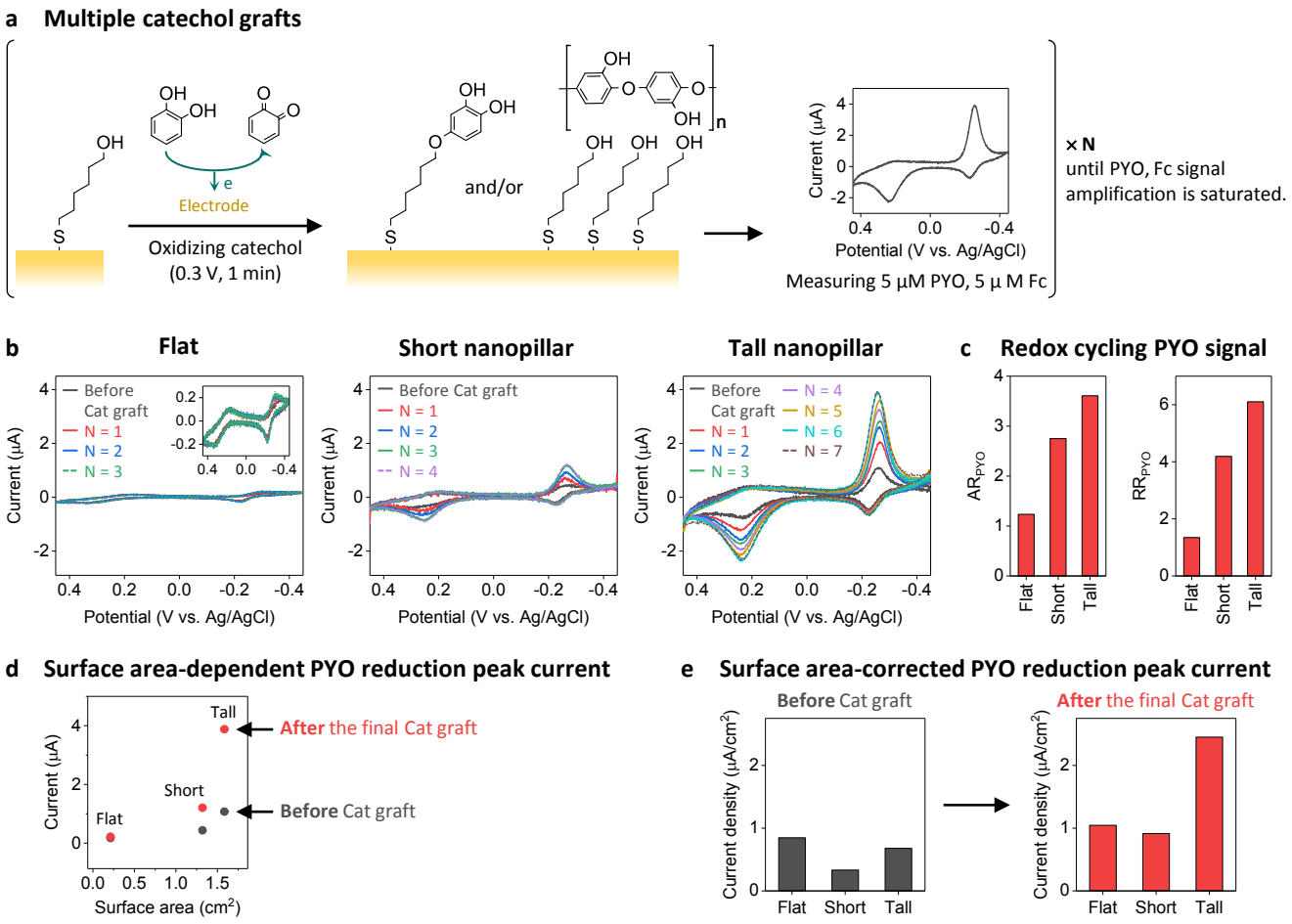

Figure 5. Electrode-dependent redox-cycling reactions. (a) *N*-times repetition of electrochemical catechol oxidation with intermittent monitoring of the PYO and Fc signals until the signal becomes saturated. **(b)** Background-subtracted cyclic voltammograms of 5 μM PYO and 5 μM Fc measured at flat (left, inset: enlarged cyclic voltammograms), short nanopillar (middle), and tall nanopillar (right) electrodes after each electrochemical catechol oxidation. **(c)** The amplification ratio (AR) and rectification ratio (RR) for the final PYO signals. **(d)** PYO reduction peak currents before the Cat graft (black) and after the final Cat graft (red) as a function of an electrode surface area. **(e)** Current densities of the PYO reduction peaks before the Cat graft and after the final Cat graft.

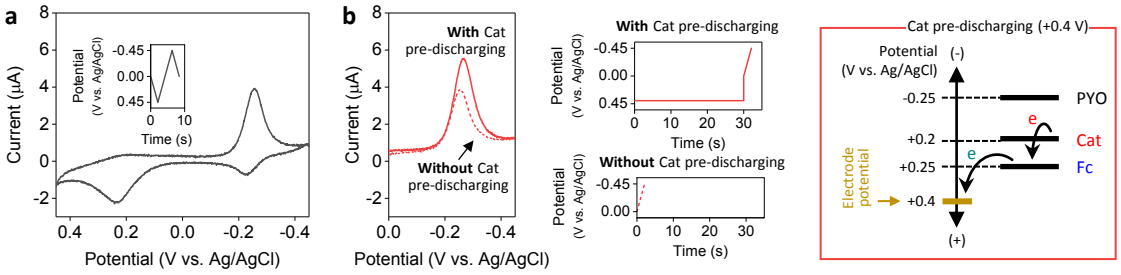

Figure 6. Electrochemical signal amplification. (a) Background-subtracted cyclic voltammograms of 5 μM PYO and 5 μM Fc at the Cat-grafted tall nanopillar electrode. The inset shows the applied potential profile over time. **(b)** Background-subtracted linear sweep voltammograms of 5 μM PYO and 5 μM Fc at the Cat-grafted tall nanopillar electrode without and with Cat pre-discharging at +0.4 V for 30 s (left) and the corresponding potential profiles (middle). Electron transfer during the Cat pre-discharging is shown in right.

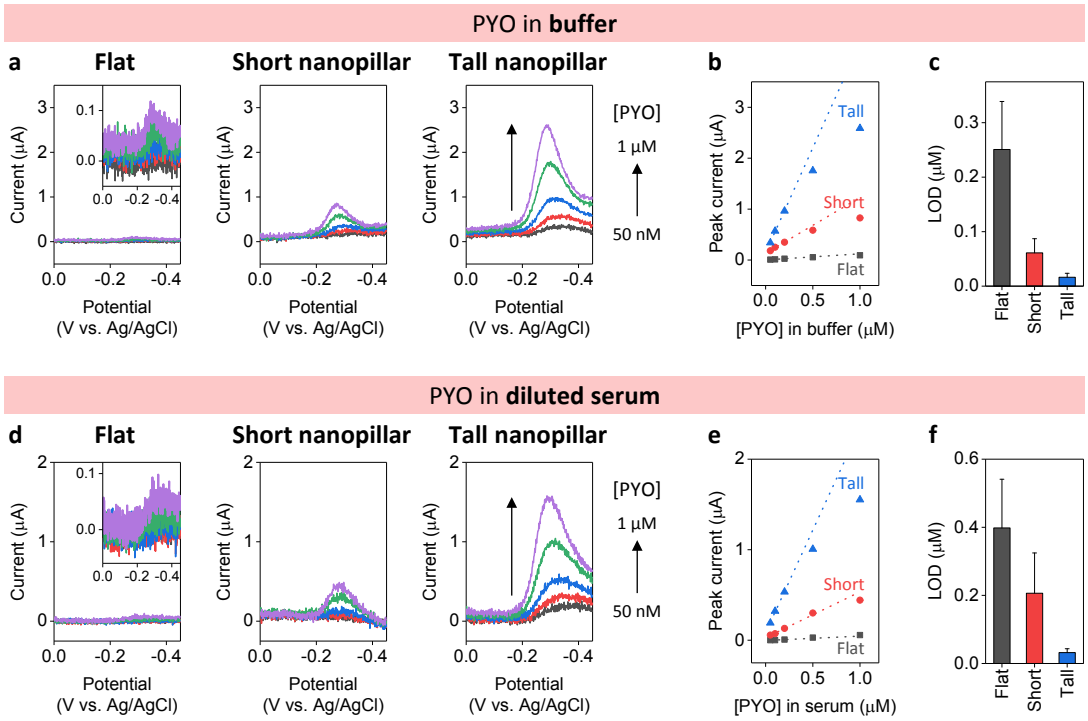

Figure 7. PYO measurement in buffered and diluted serum solution using the Cat-grafted flat, short nanopillar, and tall nanopillar electrodes. (a,d) Background-subtracted linear sweep voltammograms of PYO and Fc (concentrations: 0.05, 0.1, 0.2, 0.5, 1 μM for each) recorded in buffered (a) and 100-times diluted serum (d) solutions. Cat pre-discharging process was conducted for 30 s. **(b,e)** PYO reduction peak currents as a function of the PYO concentration. Dotted lines are the linear fitting results for the low-concentration regions. **(c,f)** Limits of detection (LODs) of the PYO measurements.

Table of Contents Entry

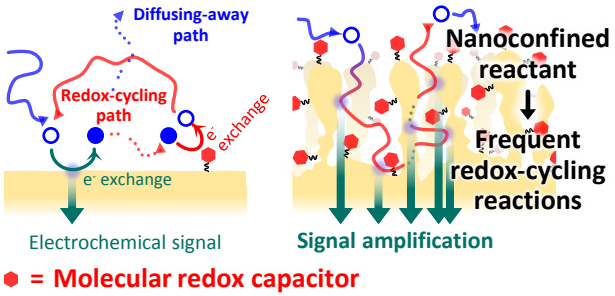

With molecular redox capacitors tethered to the electrode surface, nanostructured electrodes amplify electrochemical signals even under the mass transport constraint.